Quantum Electronics **39** (4) 321 – 327 (2009)

INTERACTION OF LASER RADIATION WITH MATTER. LASER PLASMA

PACS numbers: 42.62.Cf; 52.38.Mf
DOI: 10.1070/QE2009v039n04ABEH013964

Effects of laser radiation on immobile and fast-moving targets

V.V. Osipov, V.V. Lisenkov, V.A. Shitov, K.E. Lukyashin

Abstract. **We have studied the effects of laser pulses up to 50 J in energy and up to 1100 μs in duration, with a rise time of $\sim$ 300 μs, on immobile and moving (linear velocity of up to 10^4 cm s^{-1}) stainless steel targets. The results indicate that, in the vapour above an immobile target, optical breakdown develops at a spot-averaged power density of 5.5×10^6 W cm^{-2}, against 7.3×10^6 W cm^{-2} in air. This undesirable effect can be eliminated even at an order of magnitude higher incident power density by rapidly rotating the target (linear velocity of $\sim$ 50 cm s^{-1} relative to the laser beam). At incident power densities in the range $(0.6-1.2)\times 10^7$ W cm^{-2} (incident powers from 12 to 24 kW), evaporation from a rotating target is intermittent. To interpret this effect, a numerical model is developed which takes into account the influence of target burning. Its predictions agree with the evaporation behaviour observed in our experiments. The thicknesses of the evaporated and molten layers are evaluated as functions of laser beam parameters and target velocity, with reference to the optimisation of laser surface processing conditions.**

Keywords: *CO_2 laser, laser plume, laser evaporation, thermal oxidation, laser surface processing*.

1. Introduction

The effects of high-power laser radiation on materials had been intensely studied up to the 1990s. The basic processes involved were identified and investigated: radiation absorption, heating, melting, evaporation, melt motion such as splashing, transport or convective flow, processes in the laser plume and others. One issue of technological importance was to make clear demarcations between different effects of laser radiation according to its energy. Each of the regimes identified was termed according to the type of the resulting near-surface plasma: laser plume, optical discharge (breakdown) in evaporated target material and optical breakdown in the gas phase. These regimes differ in appearance. The plasma plume has the form of a highly luminous jet of evaporated target material strictly perpendicular to the target surface. During an optical discharge, the laser plume has an asymmetric plasma finger parallel to the laser beam. The plasma resulting from an optical breakdown in the gas phase is almost fully concentrated around the laser beam. In early studies, systematised in a number of books [1 – 7], most attention was paid to the effects of laser radiation on immobile or slowly moving targets.

Subsequently, research effort was focused on the effects of high-power, ultrashort laser pulses. In recent years, however, rapid advances in nanotechnology have revived interest in the study of the effects of high-power laser exposure on materials with the aim of devising high-output processes for the synthesis of nanostructures: clusters, fullerenes, nanoparticles, nanotubes, nanofilms and others. The development of high-output nanotechnologies typically involves the use of high-average-power laser exposure. At the same time, the use of high-power lasers for this purpose presents serious difficulties related to the development of a low-threshold optical breakdown near the target surface. In particular, CO_2 laser irradiation causes a breakdown even at power densities of $\sim 10^7$ W cm^{-2} [6]. We believe that this problem can be obviated by rapidly scanning the beam over the target.

The purpose of this work was to study the effects of high-power CO_2 laser radiation on a target when the laser beam rapidly moves over the target surface in different ways.

2. Experimental

Our experiments were aimed at examining the effects of laser radiation on immobile and rotating targets. The experimental setup used is shown schematically in Fig. 1.

CO_2 laser beam (*1*) was focused by KCl-lens telescopic system (*2*) and rotatable mirror (*3*) onto disc (*4*) mounted on a purpose-designed drive. The beam produced laser plume (*5*) above the disc surface. Its luminescence signal was recorded using photoelectronic detector (*6*) and two-channel oscilloscope (*8*). The electrical signal from the detector was fed to the oscilloscope through logarithmic amplifier (*7*), which had a high gain for small signals and a low gain for large signals. The radiation source used was a repetitively pulsed electroionisation CO_2 laser, whose design and parameters were described in detail elsewhere [8].

In our experiments, the laser was operated in the single-pulse regime, with a peak power of up to 70 kW, pulse width of 800 μs, rise time of up to 500 μs and pulse energy of up to

V.V. Osipov, V.V. Lisenkov, V.A. Shitov, K.E. Lukyashin Institute of Electrophysics, Ural Branch, Russian Academy of Sciences, ul. Amundsena 106, 620016 Yekaterinburg, Russia; e-mail: plazma@iep.uran.ru

Received 2 September 2008
Kvantovaya Elektronika **39** (4) 321 – 327 (2009)
Translated by O.M. Tsarev

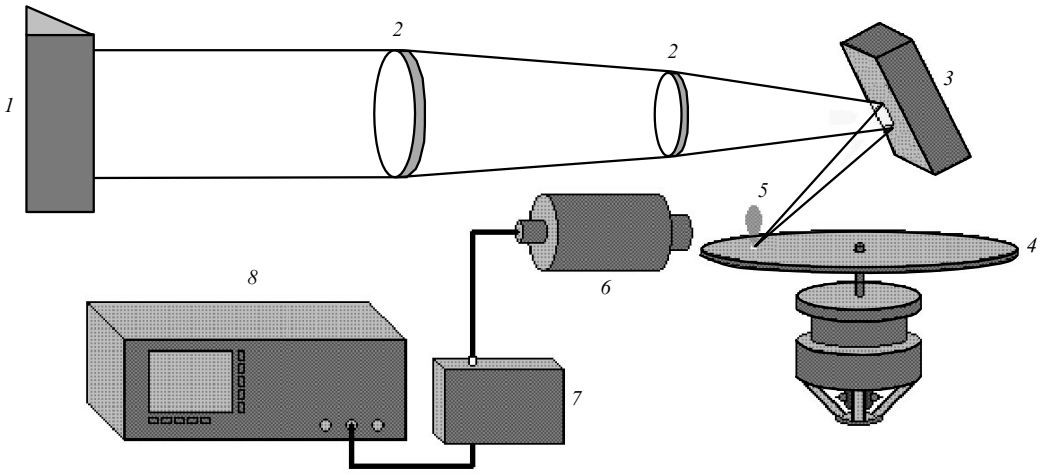

Figure 1. Scheme of the experimental setup: (*1*) CO_2 laser, (*2*) focusing KCl lens system, (*3*) rotatable mirror, (*4*) rotating target (steel disc), (*5*) plasma plume, (*6*) FEK-29 SPU-M detector, (*7*) logarithmic amplifier, (*8*) Tektronix TDS520 oscilloscope.

50 J. The target material was the most widely used stainless steel, 12Kh18N10T. The disc was 200 mm in diameter and was rotated by a motor at up to 400 rps.

The telescopic system consisted of two KCl lenses, 10 and 6 cm in diameter, with focal lengths of 90 and 30 cm, respectively. The distance between the lenses was adjusted so as to minimise the focal spot diameter (0.5 mm). The power density distribution across the spot was evaluated from the shape of the crater produced on organic glass. The experiments were conducted in air at atmospheric pressure and room temperature.

In the case of an immobile target, the laser beam was incident on the surface of the stainless steel disc at 45°. Laser pulses were always directed to a virgin zone: after each pulse, the disc was rotated through a small angle. The plasma generated near the disc surface was photographed with a Lumix DMC-FZ10 digital camera using a KS-17 optical filter (transmission range 660–2700 nm). The exposure time was 33.3 ms.

Figure 2 shows time-integrated photographs of the plasma plume ejected from an immobile target at different power densities. It can be seen that, at low incident power, the laser plume is normal to the disc surface. Its shape is unstable because of the instability of the plasma–gas interface due to the development of the Taylor instability [9]. The plume height and luminescence intensity increase with incident power. At a spot-averaged power density of 5.5×10^6 W cm^{-2}, a part of the laser plume is parallel to the laser beam (Fig. 2b), which is commonly attributed to the development of a low-threshold optical discharge (breakdown) [6]. This average power density is in reasonable agreement with previous experimental data [10].

As the incident power is raised further, the plasma zone parallel to the beam becomes brighter (Fig. 2c), and eventually it dominates (Fig. 2d). The formation of the laser plume and the development of optical breakdown are accompanied by ejection of melt droplets and pieces of the solidified film from the surface of the melt pool [11]. Their amount is unstable (Fig. 2d) and seems to be determined by the structure of the surface exposed to the laser beam, but there is a clear tendency for their amount to increase with incident power density, all other factors being the same.

Rotation of the disc, whose linear velocity relative to the laser beam was 50 m s^{-1}, drastically changed the situation: no low-threshold optical breakdown developed even at power densities an order of magnitude above the threshold (Fig. 2e). However, in contrast to what occurred in the case of an immobile target, the laser plume was deflected from the normal to the surface, presumably by the centrifugal force.

In addition, we observed an interesting effect of the laser beam on the target, which cannot be understood in terms of existing models (Fig. 3). At average power densities in the focal spot from 0.8×10^6 to 5.5×10^6 W cm^{-2}, the laser

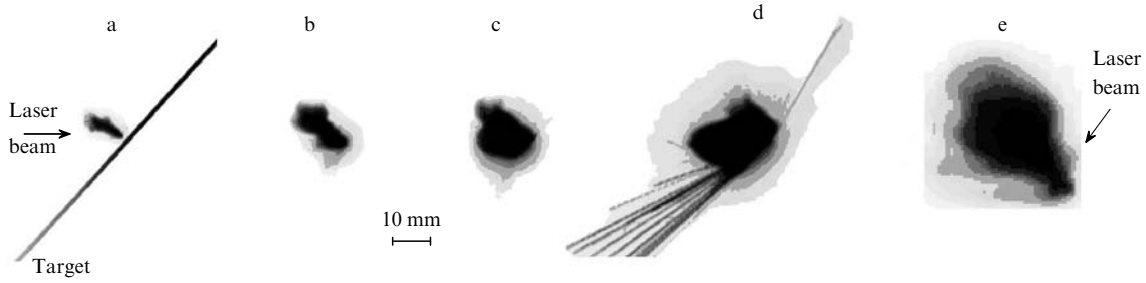

Figure 2. Photographs of the plasma plume above (a–d) immobile and (e) rotating targets; average incident power density of (a) 2.1×10^6, (b) 5.5×10^6, (c) 6.2×10^6 and (d) 7.3×10^6 W cm^{-2}.

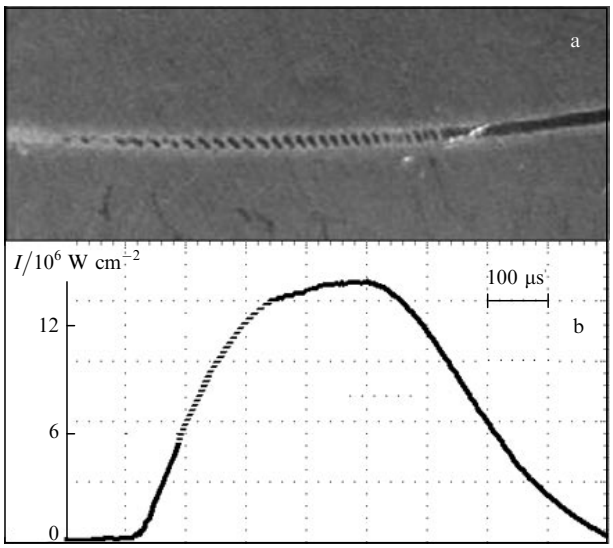

Figure 3. (a) Photograph of the groove on the target surface. (b) Oscilloscope trace of the laser pulse; the broken portion of the curve corresponds to the region shown above.

beam produced a continuous groove. At higher incident power densities, up to 1.3×10^7 W cm^{-2}, the groove was discontinuous, suggesting intermittent evaporation regime, referred to as a 'pulsating plasma generator' [6]. Surprisingly, the groove was again continuous at still higher incident intensities.

Transitions from one evaporation regime to another occurred both at the leading and trailing edges of laser pulses in the power density range indicated above (5.5×10^6 to 1.3×10^7 W cm^{-2}), corresponding to incident powers from 12 to 24 kW. Moreover, intermittent evaporation was observed during the flat top of the pulses if the incident power density was within 7.0×10^6 W cm^{-2}. To gain insight into the mechanism of this effect, the following experiments were performed:

1. We detected the luminescence of the disc surface at the beam spot (using the FEK-29 SPU-M, logarithmic amplifier and oscilloscope). The pulsation of the signal in the oscilloscope trace was found to correlate with the formation of black dots on the stainless steel surface. Consequently, the effect under consideration is related to near-surface plasma generation rather than to chemical reactions.

2. The disc surface was blown with air at the beam spot. To this end, a 1-mm-diameter nozzle was mounted 5 mm from the focal spot. The air flow velocity at the nozzle output was up to 340 m s^{-1}. This, however, had no significant influence on the beam-target interaction: the groove structure remained unchanged.

3. We used targets furnace-annealed under atmospheric pressure at 300 °C for 3 h, which produced a dense oxide film on their surface. The groove produced by subsequent laser exposure was continuous.

These results suggest that the main reason for the formation of a discontinuous groove is burning of the target material. This process may be unstable under certain conditions.

To interpret our results, we performed numerical simulations.

3. Modelling of the radiation effect on targets

Our model rests on the three-dimensional (3D) heat equation

$$c(T)\frac{\partial T}{\partial t} = \nabla(\kappa(T)\nabla T) + Q_{\text{in}}, \tag{1}$$

where c is volumetric heat capacity; κ is thermal conductivity; and Q_{in} is the internal heat source. To simplify the problem, κ was taken to be temperature-independent. The heat equation then has the form

$$\frac{\partial T}{\partial t} = \chi(T)\Delta T + \frac{Q_{\text{in}}}{c(T)}, \tag{2}$$

where $\chi = \kappa/c$ is thermal diffusivity.

A laser beam travelling along the z axis and striking the xy surface of a target creates a 3D heat source with a power density

$$Q_{\text{in}} = \alpha I(x, y, z, t), \tag{3}$$

where α is the absorption index of the laser radiation;

$$I(x, y, z, t) = A[T_{\text{s}}(x, y)]I_0(x - vt, y)\exp(-\alpha z) \tag{4}$$

is the beam intensity distribution;

$$A = 1 - R \tag{5}$$

is absorptance; R is reflectance; $I_0(x, y)$ is the intensity distribution in the focal spot; and T_{s} is the temperature on the target surface. According to Prokhorov et al. [6], $A(T)$ can be determined as

$$A(T) = A(T_0)\frac{r(T)}{r(T_0)}, \tag{6}$$

where $r(T)$ is the resistivity of the metal and T_0 is the initial (room) temperature. The $I_0(x, y)$ distribution is illustrated in Fig. 4. It corresponds to an annular profile of the focal spot on the target. The annular intensity profile is due to the use of an unstable telescopic resonator in our laser. Also presented in Fig. 4 is the geometry of the problem. The laser beam moves over the target surface along the x axis with velocity v.

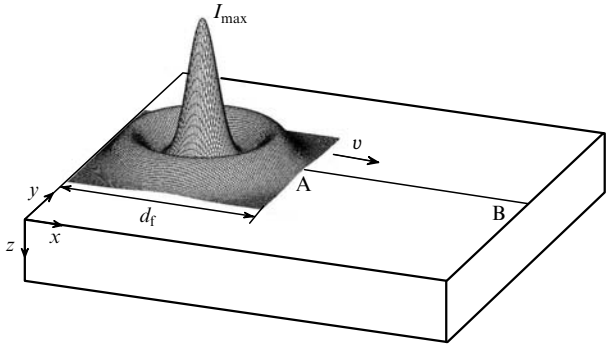

Figure 4. Geometry of the problem and intensity distribution in the focal spot; AB is the line along which the intensity peak travels, and $d_{\text{f}} = 1$ mm is the characteristic spot size.

Using the above model, we endeavoured to understand the mechanism of intermittent evaporation from the surface of a rotating target. We believe that this is related to an oxidation reaction. This process, activated by sufficiently high temperatures, makes a considerable contribution to the energy balance, assisting in the heating of the target to the boiling point of its material. Active evaporation leads to the formation of a laser plume consisting of evaporated target material with a pressure above 1 atm. The plume is capable of expelling the air from the space above the target surface, thereby preventing oxygen from reaching the surface.

If, without oxidation-induced heat release, the incident power is insufficient for evaporation, the removal of the target material ceases. Without feeding, the plume disappears, and oxygen regains access to the target surface. These processes result in intermittent evaporation. At sufficiently high incident power densities, active evaporation is possible with no contribution from oxidation, and the process is continuous.

To simulate intermittent evaporation, the simulation algorithm was provided with the capability to interrupt the oxidation reaction after the onset of active evaporation and to turn it on after plume dispersal. Unfortunately, accurate simulation of laser plume dynamics in this situation is only possible in a 3D hydrodynamic model, so we had to evaluate the plume dispersal time from experimental data.

The simulation results are illustrated in Fig. 5, which shows ablation pits on the target surface in the system of coordinates specified above. The dark areas represent pits (no deeper than 1 μm) produced by evaporation and ejection of the target material. Shown for comparison (on the same scale) are photographs of laser-processed surfaces (top images). It is seen in Fig. 5a that laser irradiation of a rotating target at an incident power of 18 kW ($I_{max} = 1.6 \times 10^7$ W cm^{-2}) produces a discontinuous groove, corresponding to the intermittent evaporation described above. At an incident power of 20 kW ($I_{max} = 1.8 \times 10^7$ W cm^{-2}), evaporation is possible without oxidation, producing a continuous groove on the rotating target (Fig. 5b). Scanning a laser beam over an immobile target at an incident power of 18 kW (without 'turning off' oxidation) also produces a continuous groove. Thus, the simulation results are in reasonable agreement with experimental data.

Therefore, to achieve stable evaporation and avoid optical breakdown at high incident intensities, the beam must be scanned over the target surface, with the target kept immobile. This process may find application in surface processing where laser machining to a small depth is needed. Because this is a topic area in laser cleaning and modification of surfaces, it is of interest to assess the effectiveness of this process and to compare it with evaporation in an immobile beam spot.

One distinction that warrants attention is that scanning the beam limits the depth of the laser heating zone in the target, in particular the melting and evaporation depths; that is, the depth of the groove produced on the target by laser evaporation, h_{ev}, drops down to zero with increasing scan velocity. The bottom of the groove is covered with a melt layer of thickness h_m, as illustrated in Fig. 6, which shows the calculated values of h_{ev} and h_m as functions of beam scan velocity at two values of I_{max} (see Fig. 4). The inset in Fig. 6 shows the section through the target along the peak intensity line (Fig. 4, line AB). The evaporation depth varies systematically with incident intensity: h_{ev} increases with increasing I_{max} and decreases with increasing scan velocity. More intriguing is the variation of the melt thickness. At scan velocities in the range 10^2 to 10^4 cm s^{-1}, where the melt thickness far exceeds or is comparable to the evaporation depth, h_m increases with increasing incident intensity and decreasing scan velocity.

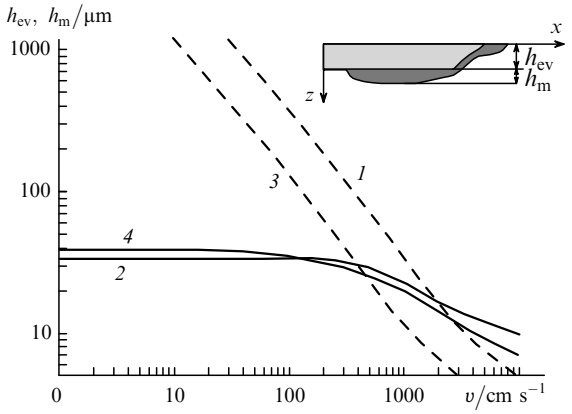

Figure 6. Calculated evaporation depth h_{ev} (dashed lines) and melt thickness h_m (solid lines) as functions of beam scan velocity v at incident intensities $I_{max} = 1.7 \times 10^7$ (*1*, *2*) and 0.7×10^7 W cm^{-2} (*3*, *4*). Inset: section of the target along line AB (see Fig. 4); the light grey and dark grey areas represent the groove and melt, respectively.

At beam scan velocities below 10^2 cm s^{-1}, h_m decreases slightly with increasing incident intensity and is independent of the scan velocity. The reason for this is that, at low scan velocities, as well as with an immobile beam spot, the melting and evaporation fronts advance into the target at the same velocity.

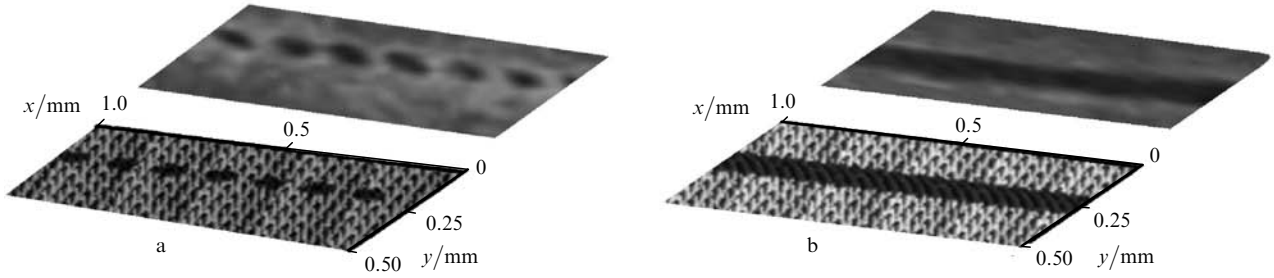

Figure 5. Shape of pits and grooves (dark areas) produced by (a) intermittent and (b) continuous evaporation: photographs (top) and simulation results (bottom).

At scan velocities above 10^2 cm s^{-1}, the h_{ev}/h_m ratio decreases markedly, attesting to a reduction in the ratio of the evaporation energy to the total energy delivered to the target, i.e. a reduction in evaporation efficiency. Figure 7 shows the evaporation efficiencies η_1 and η_2 in terms of incident and absorbed energies, respectively:

$$\eta_1 = W_{ev}/W, \tag{7}$$

$$\eta_2 = W_{ev}/W_a, \tag{8}$$

where the evaporation energy W_{ev}, incident energy W and absorbed energy W_a are per unit groove length (hereafter, per millimetre).

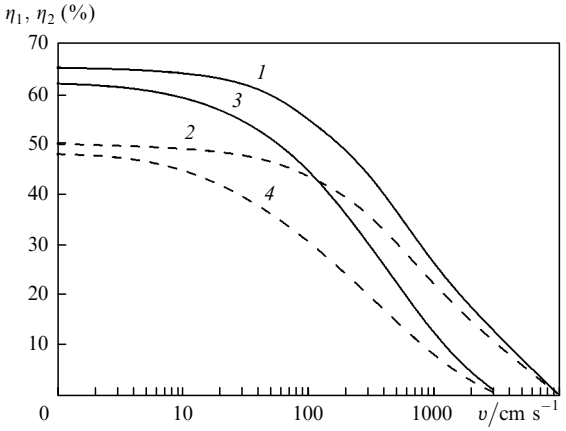

Figure 7. Calculated evaporation efficiencies in terms of incident [(*1*), dashed lines] and absorbed [(*2*), solid lines] energies as functions of beam scan velocity v at incident intensities $I_{max} = 1.7 \times 10^7$ (*1*, *2*) and 0.7×10^7 W cm^{-2} (*3*, *4*).

W_{ev}, W and W_a were determined as

$$W_{ev} = V_{ev}\Delta H_{ev}, \tag{9}$$

$$W = \int\int\int I_0(x, y, t)\mathrm{d}x\mathrm{d}y\mathrm{d}t, \tag{10}$$

$$W_a = \int\int\int A(T_s(x, y, t))I_0(x, y, t)\mathrm{d}x\mathrm{d}y\mathrm{d}t, \tag{11}$$

where $I_0(x, y, t) = I_0(x - vt, y)$; ΔH_{ev} is the volumetric heat of vaporisation; and V_{ev} is the volume of the evaporated material per unit groove length. Integration with respect to x and y was performed over the unit groove length (1 mm) and over the spot diameter, $d_f = 1$ mm (Fig. 4), respectively, and the time integration interval was $t = d_f/v$.

Our calculations indicate that, at beam scan velocities below 10 cm s^{-1}, the evaporation efficiency varies insignificantly. At higher scan velocities, the efficiency decreases, with the steepest drop above 10^2 cm s^{-1}, where, as pointed out above, h_{ev} is comparable to or smaller than h_m. In addition, it is seen in Fig. 7 that, at the lower incident intensity [curves (*3*), (*4*)], the sharp drop in evaporation efficiency begins at lower scan velocities in comparison with the higher incident intensity curves (*1*), (*2*)].

Thus, at high beam scan velocities, surface cleaning (evaporation of a layer less than 100 μm in thickness) requires much higher power levels in comparison with laser cutting and drilling, where the material is evaporated from larger depths but at a slow rate. At the same time, if high-speed surface machining is needed, it is of interest to find ways of enhancing the efficiency of this process.

First of all, one should make a demarcation between slow and rapid evaporation conditions. In the former instance, heating and melting of the target are not accompanied by significant material ejection during evaporation. This regime is well suited for various surface modification processes (quenching, doping and others). In the latter instance, sufficiently high incident intensities lead to active evaporation and the formation of a laser plume, resulting in significant material removal. This regime is typically used in laser cutting and welding, as well as in surface cleaning at small evaporation depths.

A formal criterion for active evaporation is that the target material vapour pressure be at least 1 atm. We examined the transition to active evaporation at scan velocities in the range 10^2 to 10^4 cm s^{-1}. In the same velocity range, we considered surface cleaning: material removal to a depth of 10 μm. This depth was chosen because it is close to the CO_2 laser wavelength and because it is of the same order as the melt layer thickness (see Fig. 6).

Curves (*1*) and (*3*) in Fig. 8 illustrate the influence of target velocity on the maximum intensity in the focal spot needed for the onset of active evaporation and material removal to a depth of 10 μm. Also shown in Fig. 8 are the dependences of the incident energy per unit groove length for the same conditions [curves (*4*), (*5*)]. It is of interest to analyse the calculated threshold intensity for active evaporation [curve (*1*)] in terms of the criterion proposed by Bunkin and Prokhorov [12] for the pulsed regime:

$$I \sim \sqrt{\chi/\tau}, \tag{12}$$

where τ is the pulse duration. In our case, $\tau \sim d_f/v$. Consequently, the threshold intensity for active evaporation must be proportional to $v^{1/2}$. Since the spot profile has the form of a central maximum surrounded by a ring (Fig. 4),

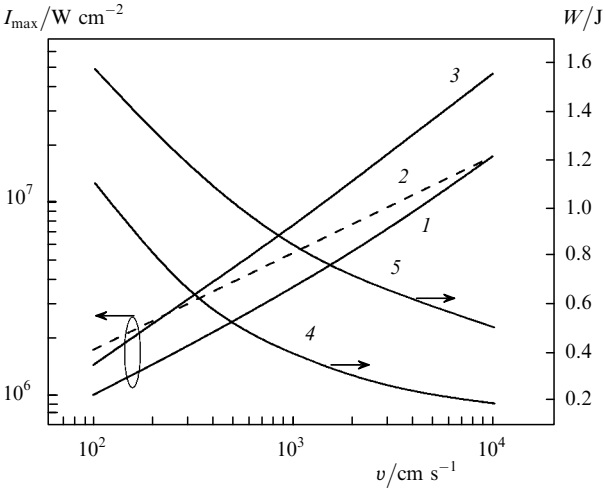

Figure 8. Calculated (*1–3*) maximum intensity I_{max} and (*4*, *5*) incident energy W [see Eqn (10)] vs. target velocity v for the (*1*, *4*) evaporation threshold, (*2*) evaporation threshold as a function of $v^{1/2}$ and (*3*, *5*) evaporation to a depth of 10 μm.

the exact value of τ is difficult to determine. It is, therefore, reasonable to qualitatively analyse our data in terms of the above criterion, i.e. to evaluate to what extent the calculated $I(v)$ curve deviates from $v^{1/2}$ behaviour. For the convenience of comparison, the $I \sim v^{1/2}$ data were represented in the form

$$I = I_1 v^{1/2}, \tag{13}$$

where I_1 is the intensity at $v = 10^4$ cm s^{-1} [Fig. 8, curve (*2*)]. The distinctions between curves (*1*) and (*2*) can be accounted for by the nonlinearity of the heat equation due to the temperature-dependent absorptance. It is also seen in Fig. 8 that, with decreasing target velocity, the threshold energy for active evaporation increases [curves (*4*), (*5*)], which is due to the increase in the melt layer thickness [Fig. 9, curve (*1*)].

In Fig. 8, the curves for the evaporation to a depth of 10 μm are similar in shape to those for the onset of active evaporation, but the intensity and energy are higher in the former case. The reduction in evaporation energy leads to an increase in evaporation efficiency with increasing target velocity [Fig. 9, curves (*3*, (*4*)]. This is due to the reduction in exposure time in a particular zone of the target upon an increase in beam scan velocity, which in turn leads to a decrease in heat absorption depth in the target. This consideration is well illustrated by the dependence of the melt thickness on target velocity for both the onset of active evaporation [Fig. 9, curve (*1*)] and the evaporation to a depth of 10 μm [Fig. 9, curve (*2*)]. Therefore, the ratio of the evaporation energy to the energy spent in heating and melting the target increases with target velocity. This is analogous to the increase in the ratios of the evaporation energy to the absorbed energy [Fig. 9, curve (*4*)] and incident energy [curve (*1*)].

This result is associated primarily with the fact that, at higher beam scan velocities, higher intensities are needed for evaporation, which, of course, requires an increase in laser output power. In surface processing, however, this may be justified by a rise in process efficiency.

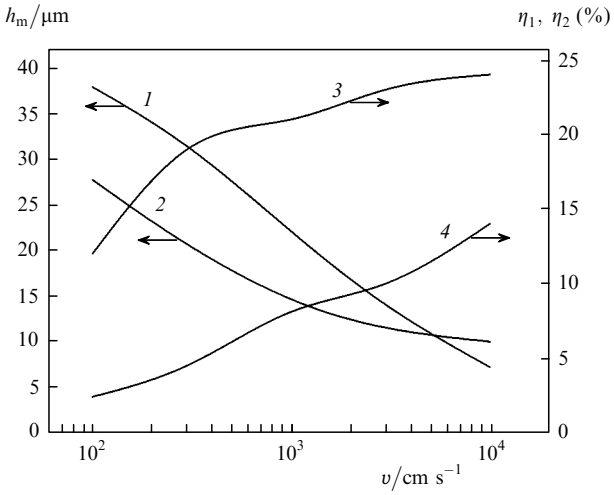

Figure 9. Calculated (*1*, *2*) melt thickness and (*3*, *4*) evaporation efficiency vs. target velocity v for the (*1*) onset of active evaporation and (*2*–*4*) evaporation to a depth of 10 μm; (*3*, *4*) ratios of the evaporation energy to the absorbed and incident energies, respectively.

The simulation results on the development of the processes responsible for intermittent evaporation also suggest that scanning a beam over an immobile target will ensure continuous evaporation. To validate this assumption, a setup was designed in which the beam was scanned over the target surface using a rotatable mirror. The target-mirror distance and the rotation rate of the mirror were adjusted so that the beam scan velocity on the surface coincided with the target velocity at the beam spot when the target was rotated. The groove thus produced was indeed continuous, which lends support to the assumptions underlying the numerical model for target evaporation assisted by metal burning.

4. Conclusions

We studied the effects of 800-μs CO_2 laser pulses with a peak power of up to 70 kW and pulse energy of up to 50 J on immobile and rotating stainless steel targets. The results indicate that, in the vapour plume above an immobile target, low-threshold optical breakdown develops at an average incident power density of 5.5×10^6 W cm^{-2}, against 7.3×10^6 W cm^{-2} in air. This effect can be eliminated by rotating the target. In particular, when the target velocity relative to the beam was ~ 50 cm s^{-1}, raising the average incident power density by almost one order of magnitude (to the maximum possible level under the conditions of our experiments, 5×10^7 W cm^{-2}) did not lead to breakdown.

At average incident power densities in the range $(0.6 - 1.2) \times 10^7$ W cm^{-2} (incident powers from 12 to 24 kW), evaporation from a rotating target was intermittent, with darker and lighter areas in the laser track.

Simulation results indicate that intermittent evaporation is only possible in the range of incident power densities where the heat released via metal oxidation makes a significant contribution to target evaporation. The reason for the intermittent character of the process is that the vapour in the forming plume expels the air, thereby preventing oxygen from reaching the target. When the plume disappears, oxidation and, accordingly, evaporation resume.

The numerical model developed for interpreting the intermittent evaporation effect provides, in addition, information necessary for optimising surface processing conditions at various target velocities, in particular, information about the evaporation depth and melt layer thickness in relation to laser beam parameters and target evaporation efficiency.

On the whole, target movement relative to the laser beam makes it possible to avoid optical breakdown, which otherwise would reduce the incident power, but leads to intermittent evaporation in a wide range of incident power densities.

Acknowledgements. This work was supported by the Russian Foundation for Basic Research (Grant No. 08-02-99056-r-ofi Ural).

References

1. Anisimov S.I., Imas A.Ya., Romanov G.S., Khodyko Yu.V. *Deistvie izlucheniya bol'shoi moshchnosti na metally* (Effects of High-Power Radiation on Metals) (Moscow: Nauka, 1970) p. 272.

2. Veiko V.P., Libenson M.N. *Lazernaya obrabotka* (Laser Processing) (Leningrad: Lenizdat, 1973) p. 191.
3. Rykalin N.N., Uglov A.A., Kokora A.N. *Lazernaya i elektronno-luchevaya obrabotka materialov* (Electron-Beam and Laser Processing of Materials) (Moscow: Mashinostroenie, 1985) p. 495.
4. Vedenov A.A., Gladun G.G. *Fizicheskie protsessy pri lazernoi obrabotke materialov* (Physical Processes Underlying Laser Processing of Materials) (Moscow: Energoatomizdat, 1985) p. 206.
5. Duley W. *Laser Processing and Analysis of Materials* (New York: Plenum, 1983; Moscow: Mir, 1987).
6. Prokhorov A.M., Konov V.I., Ursu I., Mikheilesku I.N. *Vzaimodeistvie lazernogo izlucheniya s metallami* (Interaction of Laser Radiation with Metals) (Moscow: Nauka, 1988) p. 535.
7. Koebner H.K. (Ed.) *Industrial Applications of Lasers* (Chichester: Wiley, 1984; Moscow: Mashinostroenie, 1988).
8. Osipov V.V., Gavrilov N.V., Bureyev O.A., Shitov V.A. *Laser Phys.*, **16**, 1 (2006).
9. Mesyats G.A., Osipov V.V., Volkov N.B., Platonov V.V., Ivanov M.G. *Pis'ma Zh. Tekh. Fiz.*, **29**, 13 (2003).
10. Kovalev A.S., Popov A.M., Rakhimov A.T., Seleznev B.V., Khropov S.M. *Kvantovaya Elektron.*, **12** (4), 713 (1985) [*Sov. J. Quantum. Electron.*, **15** (4), 468 (1985)].
11. Osipov V.V., Solomonov V.V., Platonov V.V., Snigireva O.A., Lisenkov V.V., Ivanov M.G. *Proc. SPIE Int. Soc. Opt. Eng.*, **6606**, 66060M (2007).
12. Bunkin V.F., Prokhorov A.M. *Usp. Fiz. Nauk*, **119**, 425 (1976).